Proceedings of ASME Turbo Expo 2011
GT2011
June 6-10, 2011, Vancouver, British Columbia, Canada

GT2011-45034

AEROELASTICITY AT REVERSED FLOW CONDITIONS - PART 1: NUMERICAL AND EXPERIMENTAL INVESTIGATIONS OF A COMPRESSOR CASCADE WITH CONTROLLED VIBRATION

Harald Schoenenborn
MTU Aero Engines GmbH
D-80995 Munich, Germany
e-mail: Harald.Schoenenborn@mtu.de

Virginie Chenaux
Ecole Polytechnique Fédérale de Lausanne
CH-1015 Lausanne, Switzerland
e-mail: virginie.chenaux@epfl.ch

Peter Ott
Ecole Polytechnique Fédérale de Lausanne
CH-1015 Lausanne, Switzerland
e-mail: peter.ott@epfl.ch

ABSTRACT

The prediction of flutter and forced response at normal flow conditions has become a standard procedure during the design of compressor airfoils. But at severe off-design conditions, the flow field becomes very complex, especially during the surge blow-down phase where reversed flow conditions occur. The correct prediction of the unsteady pressures and the resulting aerodynamic excitation or damping at these conditions remains an extremely challenging task. In the first part of the paper, basic investigations for these flow conditions are presented. Aeroelastic calculations during compressor surge are shown in the second part.

Experimental investigations were performed in the Annular Test Facility for non-rotating cascades at EPF Lausanne. The test cascade was exposed to flow conditions as expected during the surge blow-down phase which is characterized by large separation regions. Measurements of the steady-state flow conditions on the blade surface, at the outer wall, upstream and downstream of the cascade provided detailed information about the steady flow conditions.

The cascade was then subjected to controlled vibration of the blades with constant amplitudes and inter-blade phase angles. Unsteady pressure measurements on the blade surface and at the casing wall provided information about the resulting unsteady flow conditions.

Analytical CFD calculations were performed. The steady flow field was calculated using a RANS code. Based on the steady-state flow field, unsteady calculations applying a linearized code were carried out. The agreement between measurements and calculations shows that the steady flow as well as the unsteady flow phenomena can be predicted quantitatively. In addition, knowing the blade vibration mode shape, which in this case is a torsion mode, the aerodynamic damping can be determined for the corresponding flow conditions.

NOMENCLATURE

c	Chord length
Cp	Dimensionless pressure coefficient
f	Frequency
IBPA	Inter-blade phase angle
Im	Imaginary Part
k	reduced frequency
LE	Leading edge
Ma	Mach-number
$\vec{n}$	Normal surface vector
p	Pressure
PS	Pressure side
$\vec{r}$	Position vector
SS	Suction side
TE	Trailing edge
v	velocity
x	axial coordinate
α	Flow angle
δ	Vibration amplitude
ξ	Local blade coordinate
Ξ	Aerodynamic damping coefficient

Subscripts

ax	axial
stat	static
tot	total
u	unsteady
1,2	cascade inlet, exit

1 INTRODUCTION

As mentioned in the abstract, aeroelastic calculations at normal flow conditions are routine work in the design phase of turbomachinery bladings. But in off-design conditions, where usually large separation regions occur and the flow conditions are very complex, only few test cases for the validation of the aeroelastic codes exist. Especially during the blow-down phase of compressor surge, which is characterized by reversed flow conditions, no data are available. Gamache and Greitzer [1] showed the flow field structures during these flow conditions based on their experimental investigations. In the present work, measurements of steady flow and unsteady pressure measurements during controlled vibration of an airfoil under reversed flow conditions are presented. They are compared to steady and unsteady CFD calculations.

In the first part of the paper, after a literature survey of aeroelasticity at off-design conditions, an overview of the test facility and the employed measurement techniques is given. Then the analytical procedure and the numerical tools are described. A comparison between the experimentally determined flow field and the analytical results is presented for both the steady and unsteady flow conditions. Finally, the aerodynamic damping is calculated for the rig conditions.

The dedicated objective of part 1 is to show that:

a) the steady flow field and

b) the unsteady pressure amplitudes and phases of vibrating blades are captured correctly for reversed flow conditions by the numerical procedure.

In the second part of the paper [2], the procedure described here is applied to real compressor surge at reversed flow conditions.

Literature off-design conditions

In literature, some aeroelastic investigations at off-design conditions are documented. Their purpose is mainly focused on how the change in flow incidence influences unsteady blade pressures and thus aeroelastic stability. These investigations are mostly experimental. More recently, some analytical aeroelastic analyses at severe off-design conditions such as stall and surge were presented.

Bölcs and Körbächer [3] investigated a 2D section of a gas turbine cascade in the annular test facility at EPFL. The blades were subjected to a travelling wave excitation with the first bending mode. Tests at normal flow conditions and at an incidence of 22° were performed. The off-design flow was characterized by a separation bubble on the suction side close to the leading edge.

In the same test facility, Carstens et al. [4] compared experimental and numerical results of a transonic turbine cascade at design and off-design flow conditions with vibrating blades in the first bending mode. They used a 2D Euler-code for the numerical analysis of the steady and unsteady flow. Whereas for the normal flow the agreement between numerical and experimental results was good, they observed strong discrepancies for the unsteady off-design conditions, where the incidence angle was changed by more than 20 degrees. The differences might be the consequence of the incapability of an Euler code to capture the steady-state flow separation at the leading edge, which strongly determines the flow on the suction side.

In reference [5] He performed experimental investigations of a linear turbine cascade with the middle blade oscillating in a torsion mode. The off-design conditions of +/-10° against the nominal inflow angle were studied. In the second part of the study [6], He provided the results from a computational study of the experiments with an unsteady, non-linear Navier-Stokes solver. The comparison between experimental investigations and calculations was satisfactory, except in the regions of flow separation.

Cinnella et al. [7] presented numerical results of the Standard Configuration test case 11, which is a transonic turbine cascade at off-design conditions. The inlet flow has an incidence of 34°, leading to a stagnation point on the pressure side and a large separation on the first 30% of chord on the suction side.

Vogt and Fransson [8] investigated an oscillating low-pressure turbine rotor blade in an annular sector cascade in order to study the mode shape sensitivity at design and off-design conditions. The acquisition of unsteady blade surface pressure data allowed them to determine aeroelastic stability data. Negative incidence caused a separation on the pressure side which was found to have a destabilizing effect on the axial bending mode, whereas edgewise modes were found to become more stable. Torsional modes are nearly not affected by the incidence change.

Vahdati et al. [9] performed an advanced 3D viscous time-accurate flow analysis of compressor stall and a surge event of a complete core compressor with application to aeroelasticity. They assessed the influence of these unsteady phenomena with the help of Fourier components of the blade forcing.

More recently, the same research group (di Mare et al., [10]) performed a numerical study of a complete surge cycle of a 6-stage high-pressure compressor, using a 3D time accurate CFD code. For various conditions (steady reversed flow, normal flow, max reversed flow, beginning of surge cycle and zero flow) they performed flutter stability computations of a rotor for several mode shapes. They found that the damping curve (aerodynamic damping vs. IBPA) has still the shape of a sine curve, but that the level of damping is largely reduced compared to normal flow conditions.

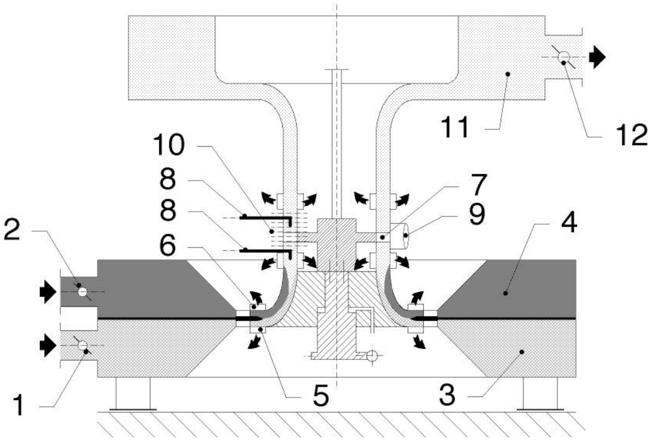

1,2	Inlet valves	9	Optical window
3,4	Settling chamber	10	Static wall pressure taps
5,6	Preswirl vanes	11	Outlet chamber
7	Airfoil	12	Outlet valve
8	Aerodynamic probes		Boundary layer suction

Figure 1: Non-rotating annular test rig

2 TEST FACILITY

Annular cascade

The test facility at the Ecole Polytechnique Fédérale de Lausanne (EPFL) has been used for numerous subsonic and transonic investigations of compressor and turbine blade geometries with vibrating blades. From the first design [11] to very recent studies ([12],[13],[14]), the test rig and its measurement equipment was improved steadily. As in those papers the test rig is described in detail, here only a short description is given which is necessary in order to understand the present work. Especially Rottmeier [12] gives a very good overview of the measurement procedures.

Figure 1 shows a cross-section of the non-rotating annular test rig. The flow is provided by an external compressor and fed into an inner and outer settling chamber (3,4). The flow rate is controlled by the inlet valves (1,2). As the blades are not rotating, the inner and outer pre-swirl guide vanes (5,6) are used to obtain a large inflow angle which should be representative for a rotating blade. Downstream of the guide vanes the flow is accelerated and turned from the radial to the axial direction. The flow passes through the test cascade (7) and leaves the rig by the outlet chamber (11) and the outlet control valve (12).

One of the most valuable features of this rig is the possibility to impose controlled vibration to the airfoils. The measuring cascade is composed of 20 independent blade vibration systems. The airfoil is fixed to a foot with a torsion mass and a torsion spring, as shown in the sketch in Figure 2.

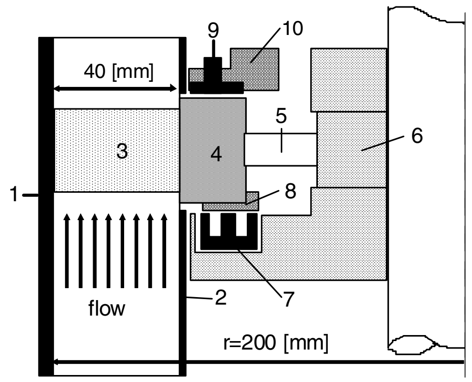

1	Outer wall	6	Hub
2	Inner wall	7	Magnetic coil
3	Airfoil	8	Transformator plate
4	Torsion mass + foot	9	Displacement transducer
5	Torsion spring	10	Vibration limiter

Figure 2: Detail of measurement section

The manufactured system is presented in Figure 3. Due to this design, all blades can vibrate independently of each other. The drawback of this design is that there are labyrinth slots all around the blades where air can be exchanged through the inner chamber of the rig. A transformator plate (8) is fixed to the torsion mass (4), which enables a magnetic excitation system (7) to move the blades (3) with constant amplitudes and a defined inter-blade phase angle. The IBPA can be adjusted in steps of 360°/20 blades = 18°. A displacement transducer (9) measures the vibration movement. Hitherto, this excitation system was only used for normal flow directions. The application to the present flow conditions is very challenging due to the high aerodynamic forces acting on the blades. This limits the vibration amplitude.

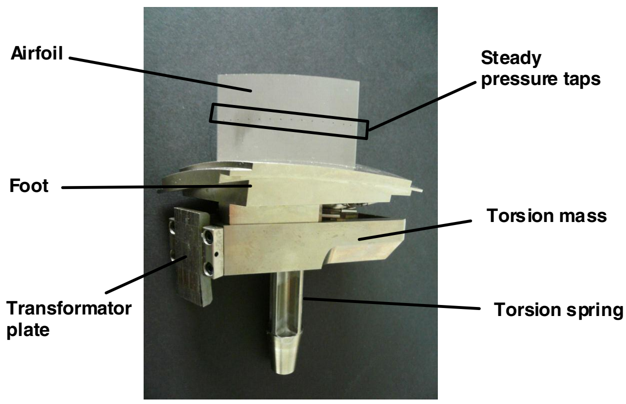

Figure 3: Manufactured blade system

Measurement equipment

The steady flow conditions upstream and downstream of the test cascade are obtained from spanwise-circumferential traverse data, measured by 5-hole aerodynamic probes (see the axial cross section in Figure 4). 15 radial positions are measured over one inter-blade channel (18°, every 1°). The probes are calibrated up to sonic Mach-numbers. Static wall pressure taps are inserted in the outer wall in order to measure the wall pressures. The pressure distribution on the airfoil is determined by static pressure taps on the blade surface.

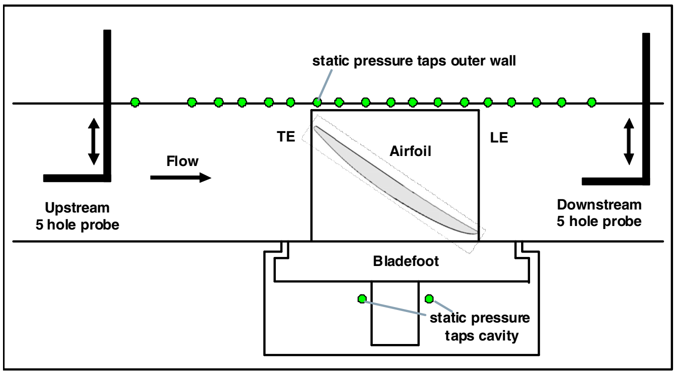

Figure 4: Instrumentation flow channel

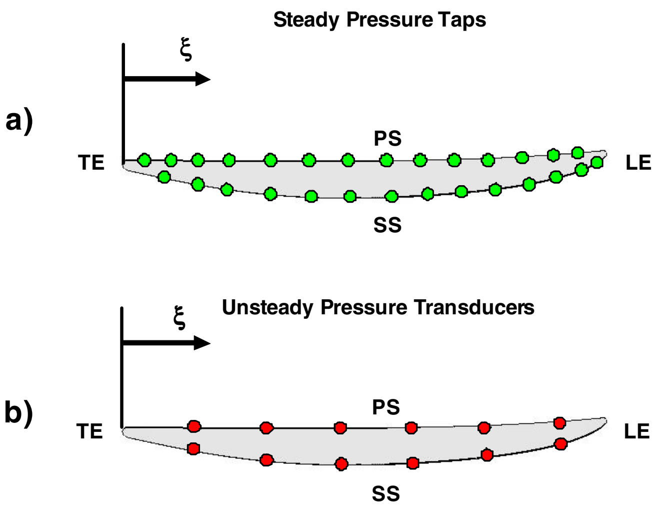

Figure 5a, b: Steady and unsteady pressure taps

In Figure 5a, the positions of the pressure taps for steady pressure measurements on the blade surface can be seen. 14 measurement positions are located on each side of a flow channel. As not all of the pressure taps could be positioned on one blade, they were distributed on two blades, one containing the suction side taps and the other the pressure side taps. In the cascade, they were arranged in a way that one flow channel could be measured, see also Figure 6.

Figure 5b shows the locations for the measurement of the unsteady pressure. Overall, 18 unsteady measurement transducers were mounted, 6 on the pressure side of blade 1, 3+3 on the pressure and suction side of blade 2 and again 6 on the suction side of blade 3 as shown in Figure 6 (view from downstream). For all measurements, the pressure taps are located at 50% of the blade span. Note that for each unsteady pressure measurement location, a corresponding steady-state pressure is include on the steady instrumented blades.

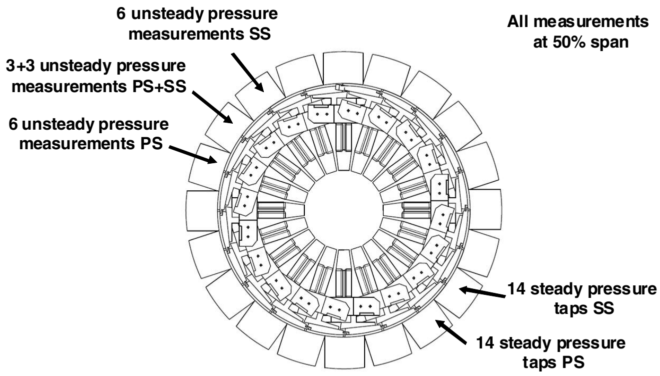

Figure 6: Distribution of pressure taps in annulus (view from upstream plane)

Table 1 finally shows a summary of the relative measurement positions. For a more detailed description of the measurement technique see reference [14].

ξ [-]	Steady Pressure			Unsteady Pressure	
No.	SS	PS	Casing	SS	PS
1	0.98	0.94	-1.07	0.90	0.90
2	0.95	0.90	-0.71	0.75	0.75
3	0.90	0.83	-0.56	0.60	0.60
4	0.84	0.75	-0.41	0.45	0.45
5	0.77	0.68	-0.27	0.30	0.30
6	0.70	0.61	-0.12	0.15	0.15
7	0.63	0.53	0.03		
8	0.55	0.46	0.17		
9	0.47	0.38	0.32		
10	0.39	0.30	0.47		
11	0.30	0.23	0.61		
12	0.21	0.15	0.76		
13	0.15	0.10	0.91		
14	0.08	0.05	1.06		
15			1.20		
16			1.35		
17			1.50		
18			1.64		

Table 1: Measurement locations

As the test rig was used for such a flow configuration for the first time, the limitations of the rig regarding inlet flow Mach-number and flow angle, which determines the mass flow rate, had to be found. Table 2 presents the measurement matrix with the operating points used in this paper. These measurement points are at the limits of the test facility for this type of flow. The achievable Mach-numbers are representative for speeds at part load surge cycles. CFD calculations are presented for the operating point 1 with Ma_1=0.2, β_1=45°.

The reduced frequency at the operating points is given by equation (1):

$$k = \frac{c/2 \cdot 2 \cdot \pi \cdot f}{v} \tag{1}$$

Case	Ma_1	β_1	k
1	0.2	45	0.80
2	0.2	70.8	0.80
3	0.5	70.8	0.34

Table 2: Measurement matrix

3 ANALYTICAL PROCEDURE

The numerical investigations are performed using the MTU standard procedure for flutter calculations. This procedure consists of the use of a linearized flow solver. For this purpose, the flow is split into a mean, steady flow and a small, harmonic perturbation. Thus, the steady flow problem is decoupled from the unsteady problem. The steady flow solution is obtained with the code described below. A linearized code is used subsequently to calculate the unsteady behavior of the airfoil. Details of this code are given after the description of the steady flow solver.

Steady Flow Solver

For the steady aerodynamic flow solution the MTU and German Aerospace Research Center (DLR) common turbomachinery numerical simulation system TRACE ([15],[16],[17]) is used. It is applied by a growing user community both in research and industry.

In this solver, under the relative frame of reference, the 3-D Reynolds averaged Navier-Stokes equations are integrated in time by a fully implicit formulation of the second-order scheme for the compressible ideal or real gas in conjunction with the two equation k-ω turbulence model, which is enhanced by DLR´s own submodels for rotation, compression and stagnation point anomaly.

The convective fluxes are discretized using the Roe's TVD upwind scheme which is combined with the van Leer's MUSCL extrapolation to obtain second- or third-order accuracy in space depending on the used limiter. The derivatives of the viscous fluxes are approximated by central differences.

For a steady multistage calculation, the nonreflecting formulation according to Giles is applied at inlet and outlet boundaries, whereas the coupling of different stages is realized by the mixing-plane approach. For more details it is referred to the above mentioned references.

Unsteady Flow Solver

The unsteady code is based on a time-linearized Euler method. The steady flow is interpolated onto a single H-grid for each passage. The time-linear unsteady flow equations are solved on a moving grid, which conforms to the motion of the airfoils for the investigated mode shape. The solution algorithm uses a cell-vertex formulation. Nonreflecting boundary conditions are employed to accurately model isolated cascades.

More details of the linearized method and its extensive validation can be found in Kahl [18] and Kahl and Klose [19]. Kahl and Hennings [20] applied this code to the unsteady calculation of a compressor cascade in the EPFL test rig under forward flow conditions.

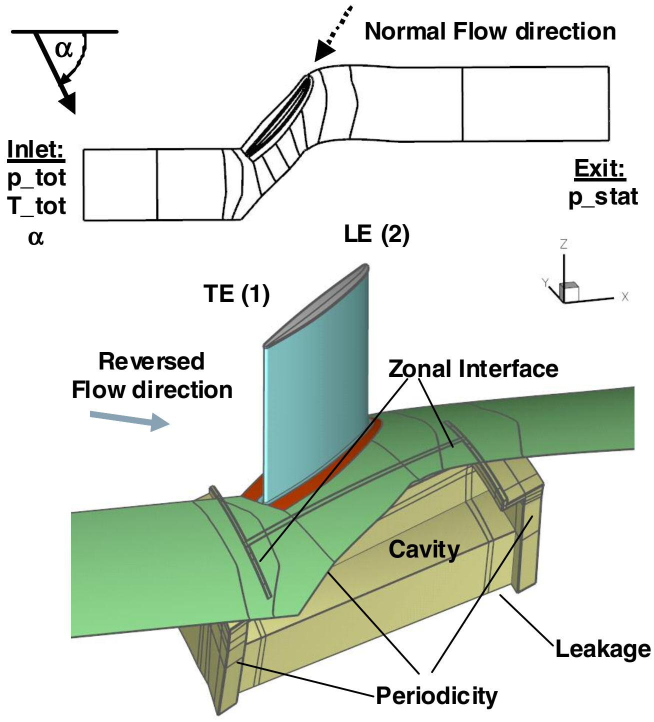

Figure 7: Computational setup

Investigation setup

In Figure 7, the computational setup is presented. The airfoil is meshed like a normal airfoil and then inlet and exit are exchanged, so that the metal trailing edge (TE, position 1) shows to the inlet. An O-type grid is placed directly around the blade surface (blue) and a C-type grid is created directly around the O-type grid (red). The remaining flow domain is meshed with H-type grids (green). An average tip clearance of 1.5% is included as measured in the rig. The distance of the inlet and exit boundaries from the cascade is shown in the upper part of the Figure. The normal forward flow direction or the airfoil is indicated by the dashed arrow.

In previous numerical studies of this annular test rig it was found that the cavity flow through the slots, which are all around the airfoil, affects the flow solution [18]. Thus, the complex cavity with the slots is included in the present model. The cavity is connected to the main flow domain by a zonal interface, which required a refined meshing in this area. At the inlet, the radial total pressure profile taken from the upstream measurements with the 5-hole probe are prescribed, together with the total temperature and the flow angle. At the exit, the averaged static pressure from the measurements is fixed, assuming radial equilibrium. As the cavity is not closed completely, but some small leakage to the exterior is present, the cavity pressure measurements are used to define additional leakage flow into the cavity.

Figure 8 shows the computational grid. The passage consists of 3.277.329 nodes and the cavity has an additional 1.006.046 nodes. Low-Reynolds treatment of the blade walls is imposed.

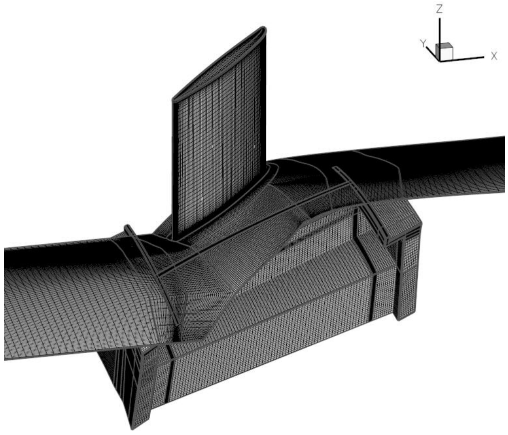

Figure 8: Computational grid

4 STEADY FLOW RESULTS

As already mentioned in chapter 3, the unsteady calculations with the linearized code is based on the steady solution. Thus, it is important to capture the steady flow field correctly. For this purpose, steady pressure taps at the casing and on the blade surface were located. For a comparison of measurements and calculations, a dimensionless pressure coefficient was calculated as follows:

$$Cp = \frac{p - p_{1,stat}}{p_{1,tot} - p_{1,stat}} \qquad (2)$$

Figure 9 shows the pressure coefficient contours of the flow field at 50% span for the case Ma_1=0.2, β_1=45°. The flow enters the cascade from the left side. The stagnation point, which is rather a broad stagnation region, is located on the pressure side close to the trailing edge (TE). A large recirculation zone can be discerned on the suction side of the blade in the trailing edge region. The flow leaves the cascade at the leading edge (LE).

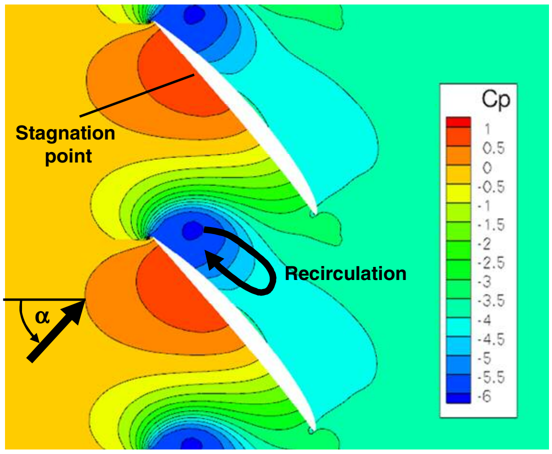

Figure 9: Steady-state flow field (Ma_1=0.2, β_1=45°)

Blade surface pressure

In Figure 10 the calculated and measured pressure coefficient (Cp) on the blade surface at 50% span is presented. The solid lines indicate the CFD solution, whereas the symbols represent the measurements. The agreement on the pressure side is perfect, on the suction side there are some small deviations between x/c_ax=0.25 and 0.55. The nearly constant pressure on the suction side up to x/c_ax=0.25 is due to the recirculation region. Measurement errors are estimated to be of the order of the size of the symbols and cannot be the reason of the differences. For the other flow cases, the agreement is similar.

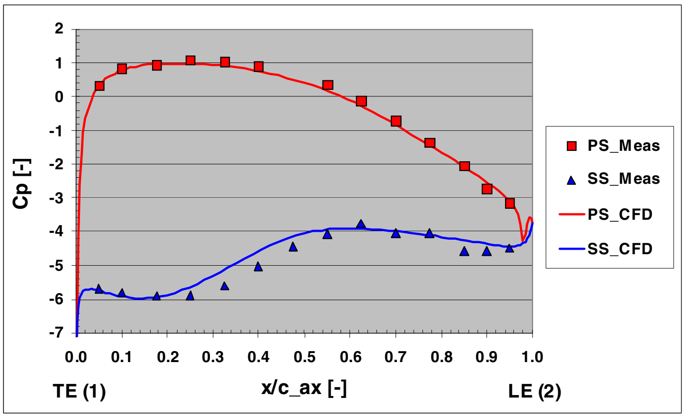

Figure 10: Blade surface pressure (Ma_1=0.2, β_1=45°)

Casing wall pressure

In addition to the blade surface pressures, the pressure taps in the casing provide another possibility to compare the calculated flow solution with measurements. In Figure 11a the calculated wall pressure coefficient contours are presented on a plane in axial and circumferential direction. The view direction is radially outward. In Figure 11b the corresponding measured values are displayed. The comparison shows a very good agreement.

In summary, the steady-state CFD calculations reproduce the complex flow field characterized by the large recirculation region with a high level of confidence.

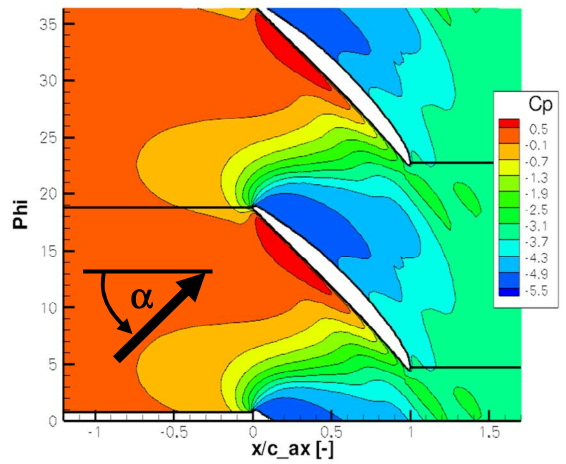

Figure 11a: Calculated wall pressure contours

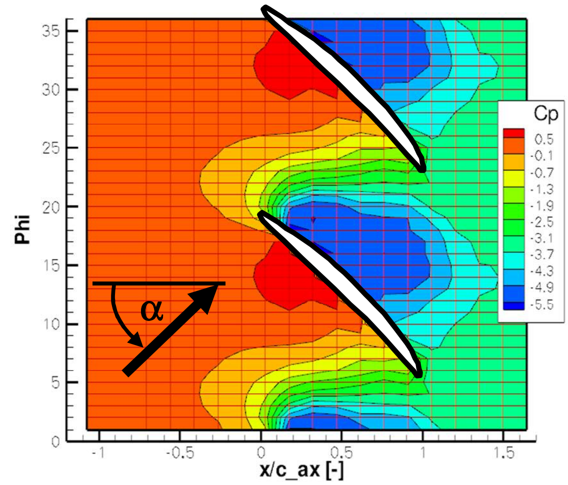

Figure 11b: Measured wall pressure contours

5 UNSTEADY FLOW INVESTIGATIONS

Based on the above described steady flow field, unsteady aeroelastic calculations with the linearized code were performed.

Unsteady blade surface pressure

After the stabilization of the flow in the test rig for a certain performance point, the cascade is subjected to controlled torsional vibration with constant amplitudes for all blades and a defined IBPA. The resulting unsteady pressure amplitudes are measured and converted to an unsteady pressure coefficient according to equation (3), where δ is the angular vibration amplitude of the blade.

$$Cp_u = \frac{|p_u|}{\delta \cdot (p_{1,tot} - p_{1,stat})} \quad (3)$$

The calculated unsteady pressure amplitudes are processed in the same manner. As shown in the second part of the paper, the IBPA's close to 180° are of special interest, thus only results for this IBPA are presented. Figure 12a shows the comparison between calculated and measured unsteady pressure coefficients for the case Ma_1=0.2, β_1=45° for an IBPA of -180°.

On the pressure side, the agreement is close. On the suction side, the agreement is good for x/c_ax larger than 0.5. Upstream, the measurements show higher values. This is the region where the large separation zone is present. Two values at the same x/c_ax-positions represent redundant measurement positions (PS+SS unsteady measuring blade). The measurement error due to calibration, repeatability, polynomial fitting, transducer acceleration and other errors is shown in the plot by the errorbar. Similar observations were made by He [6] in his computational study, where the unsteady pressure amplitude was underpredicted in the region of separated flow, probably due to the linearized approach.

It turned out that for the present flow conditions the forces onto the blades are much higher than for normal flow conditions and that for this reason it was not possible to obtain torsional vibration amplitudes as high as for normal flow conditions. Thus, the achievable unsteady pressures are small and the relative error higher than desirable. Furthermore, the quality of the unsteady signals on the suction side is not as reliable as on the pressure side. This may be due to the influence of the large recirculation zone.

In Figure 12b the corresponding phases for case 1 are shown. Larger deviations occur on the suction side closer to the TE and at the first point on the pressure side at x/c_ax=0.1. Otherwise, the agreement is satisfactory.

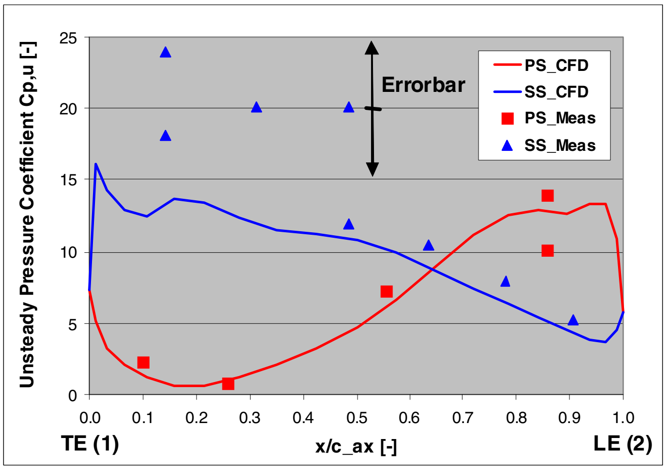

Figure 12a: Unsteady pressure coefficient case 1, IBPA=-180°

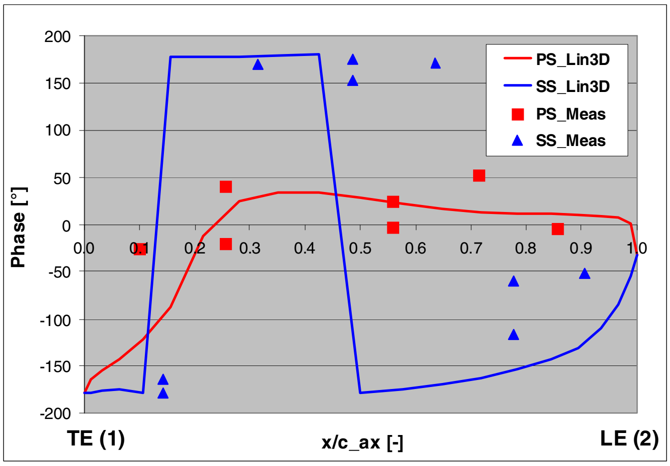

Figure 12b: Phase case 1, IBPA=-180°

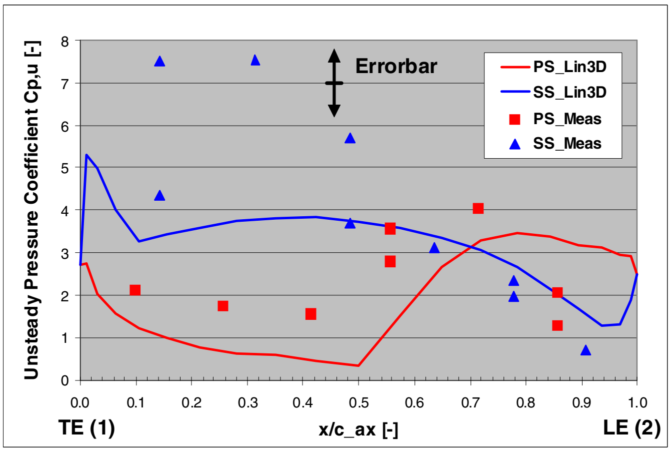

Figure 13a: Unsteady pressure coefficient case 3, IBPA=-180°

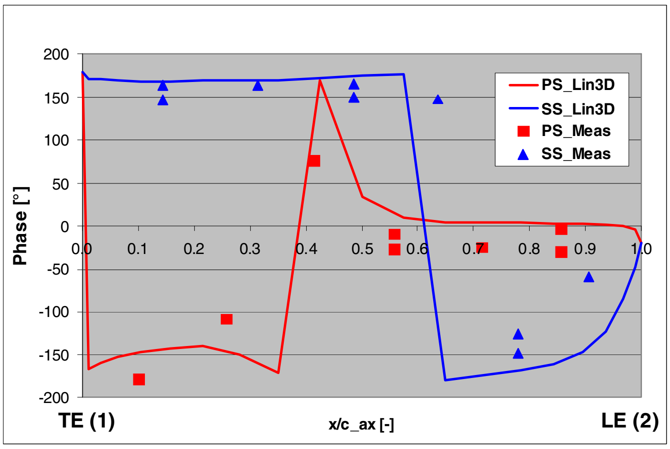

Figure 13b: Phase case 3, IBPA=-180°

In Figure 13a, the unsteady pressure coefficient of case 3 is displayed. Here, the agreement on the pressure side is not as good as for case 1. In the range x/c_ax = 0-0.7, the pressure is underpredicted, while in the remaining part it is overpredicted with respect to the measurements. On the rear part of the suction side, the agreement is good. In the front part, there are again large deviations between some unsteady pressure transducers. The agreement for the phase for case 3, presented in Figure 13b, is very good.

Figure 14 shows two examples of a FFT of the unsteady pressure signals for case 1 on the pressure side at x/c_ax=0.85 (left hand side) and on the suction side at x/c_ax=0.5 (right hand side). While the signal on the pressure side shows a clear peak at the vibration frequency (normalized frequency = 1), the signal on the suction side does not show a unique frequency response. In addition, due to the limited vibration amplitude the relative measurement error for the unsteady measurements is much higher than for the steady measurements. Keeping these aspects in mind, the comparison of the unsteady pressure coefficients is quite good, with discrepancies in the recirculation region.

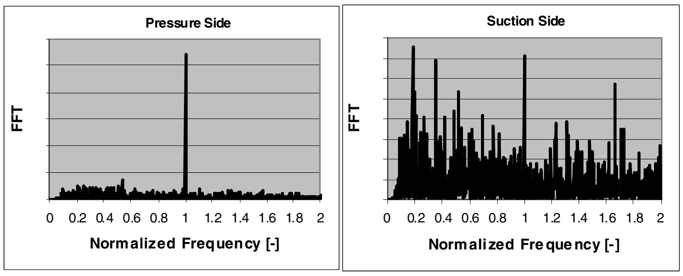

Figure 14: FFT of unsteady pressure signals (left = pressure side, right = suction side)

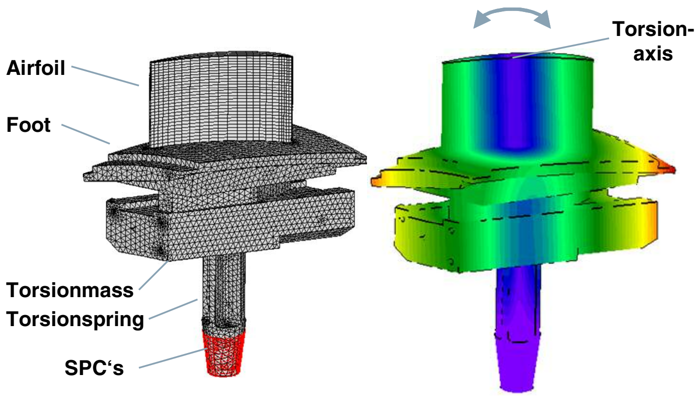

Figure 15: FEM model and mode shape

Vibration mode shape

For the determination of the aerodynamic damping the mode shape of the blade has to be calculated. Figure 15 shows the FEM-model of the blade assembly with the torsion spring, the torsion mass, the blade foot and the blade itself on the left hand side. The torsion spring is fixed in the hub with a screw so that the boundary conditions with single-point constraints (SPC's) at the red nodes, as indicated in the Figure, can be applied. The resulting torsion mode shape is presented on the right hand side. The Young's modulus of the material was adapted so that the frequency met the measured frequency of a ping test. The mode is a rigid body mode for the blade, since all the movement takes place in the torsion spring. For the calculation of the aerodynamic damping, the grid surface displacements of the FE grid for this mode shape are mapped onto the CFD mesh.

Aerodynamic damping

First, for a comparison between the calculations and measurements, the global stability of the configuration is determined by a normalized overall aerodynamic damping coefficient, which is based on the pressure and phase distribution at 50% span of the blade. A normalized value according to Beretta [21] is calculated in eq. (4)

$$\frac{\Xi}{\Xi_{ref}} \sim \mathrm{Im}\left(\oint_S C_{p,u} \cdot \left[(\vec{r}-\vec{r}_0)\times\vec{n}\right]\cdot ds\right) \qquad (4)$$

where $\vec{r}$ is the position vector of the unsteady pressure transducer or grid point and $\vec{r}_0$ corresponds to the vector of the torsion center. $\vec{n}$ is the surface normal vector and ds is a surface element, which may become quite long for the experimentally determined values. Table 3 summarizes the values for case 1&3 for an IBPA of -180°. The deviation of 10% (29%) is considered to be quite good, taking into account the relatively large measurement uncertainties on the experimental side and the difficult flow conditions and the linearized Euler solver on the numerical side.

Case	Lin3D	Meas	Deviation
1	0.693	0.988	29%
3	0.296	0.327	10%

Table 3: Normalized overall aerodynamic damping coefficient

In order to get an impression of the aerodynamic damping over a larger range of operating conditions and IBPA, in Figure 16, the calculated local excitation, which is equal to the negative damping, on the blade surface for the case Ma_1=0.2, β_1=45° and an IBPA of -180° is presented. The reversed flow direction is indicated by the arrow creating the stagnation region at the TE of the pressure side. The aerodynamic damping is calculated in terms of the logarithmic decrement. It should be noted that due to confidentiality reasons, only normalized values (divided by a not disclosed reference aerodynamic damping) are presented.

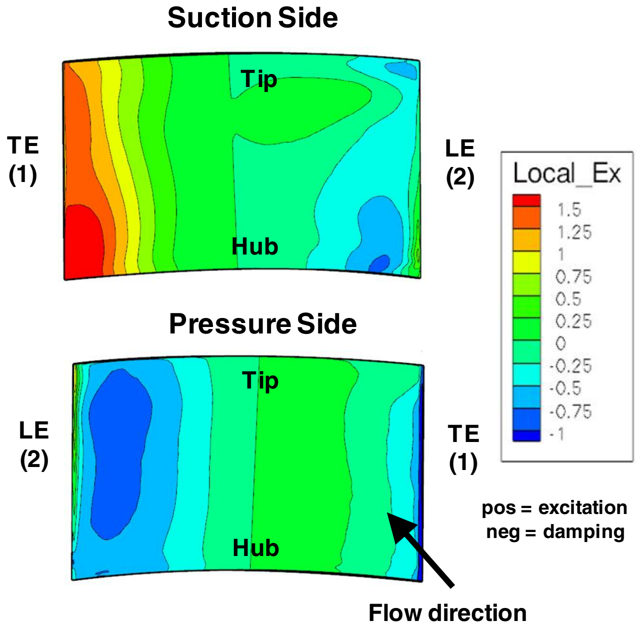

Figure 16: Local excitation blade surface

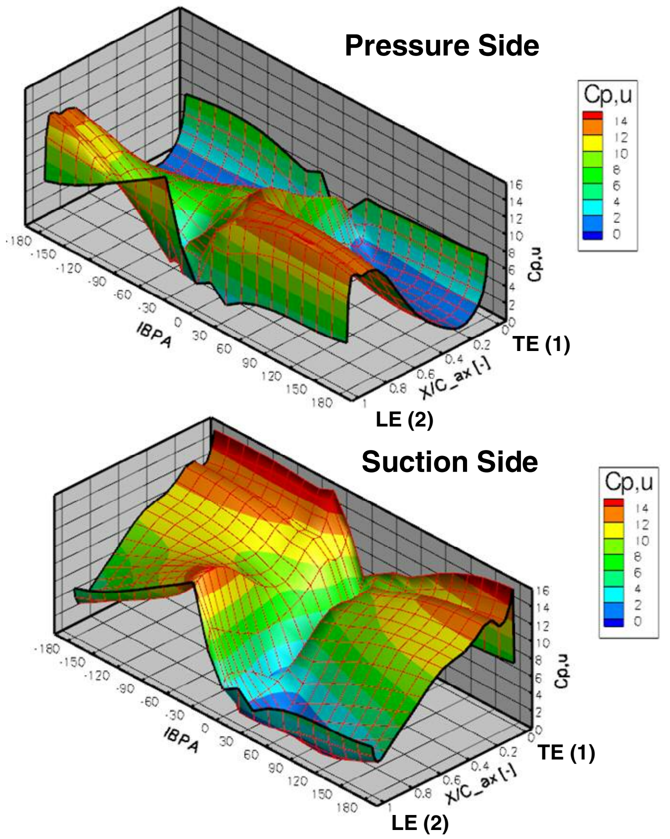

Figure 17a: Calculated unsteady pressure coefficient for all IBPA of case 1

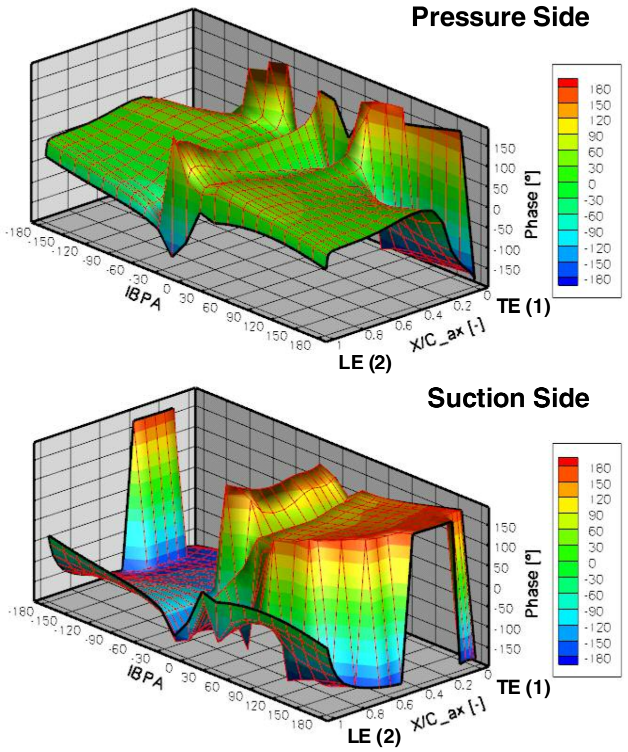

Figure 17b: Calculated phases for all IBPA of case 1

In the region between approximately 20% span and 80% span the distribution is quite 2-dimensional, whereas close to the tip and hub 3-dimensional effects due to the tip vortex and the leakage flow around the blade foot become important. It can also be seen that at the trailing edge of the suction side a negative damping (excitation) prevails. This is the region with the large separation. The leading edge regions show a positive damping. The integral value over the complete surface determines if the blade is stable or unstable for this special flow condition.

The distribution of the calculated unsteady pressure coefficient along the blade chord for all IBPA for the case Ma=0.2, 45° is presented in Figure 17a. It can be seen that for a wide range of IBPA (-180° to -90° and +60° to 180°) the pressure coefficients look quite similar and have nearly the same values. At the trailing edge (x/c_ax=0) the unsteady pressure coefficient is low on the pressure side and highest on the suction side. Approaching the leading edge (x/c_ax=1), this effect is reversed. Between -90° to +60°, and especially at 0°, the pressure coefficient looks different. While it is close to zero on the suction side along the whole blade, it is much higher on the pressure side.

In Figure 17b, the corresponding phases are shown for all IBPA. On the pressure side, the phases are close to 0° over a very broad range of IBPA and x/c_ax = 0.2-1. Only close to the trailing edge and at an IBPA around 0 the phases are considerably different. On the suction side, the phases are close to 180° over a broad range of IBPA and x/c_ax=0-0.8. Only close to the leading edge the phases approach 0°. Some higher differences can be observed again around an IBPA=0°.

Finally, in Figure 18 a comparison of the calculated normalized aerodynamic damping for the three different performance points of Table 2 is displayed. The red curve represents the case Ma_1=0.2, β_1=45°, which has been discussed extensively in the previous sections. The black curve shows the case with the same Mach-number, but a higher inlet angle. The blue line represents the maximum Mach-number with the high inlet angle. At the missing points of the blue curve the calculations did not converge, which is not unusual. Even for normal flow conditions, some points on a flutter curve may not converge due to numerical reasons.

A higher inlet angle (red compared to black) results in a higher minimum aerodynamic damping and a smaller spread of the curve. A higher Mach-number at the same inlet angle (blue compared to black) gives a lower minimum aerodynamic damping, which, in this case, even becomes negative.

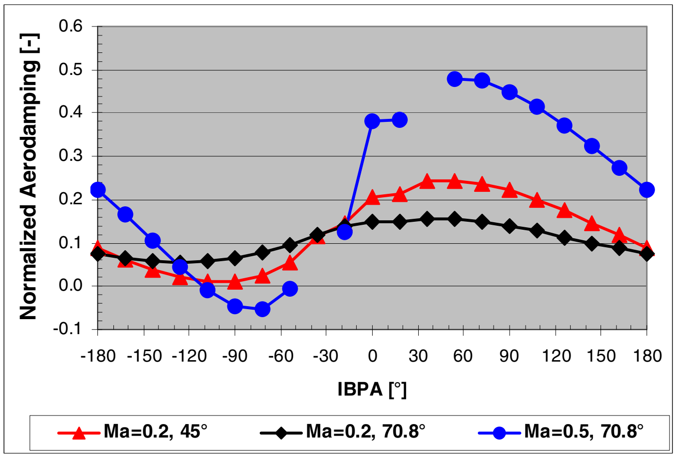

Figure 18: Normalized aerodynamic damping for different operating points

6 SUMMARY AND CONCLUSIONS

The work is summarized below and appropriate conclusions are drawn from the investigations:

- A compressor cascade was tested at reversed flow conditions as they may occur during the surge blow-down phase. The cascade was instrumented in order to measure the steady flow field,as well as the steady-state and unsteady blade surface pressures at 50% span, during controlled vibration.
- Accompanying steady and unsteady CFD calculations were performed.

- The steady CFD calculations, which are a basis for the linearized unsteady calculations, match the measured flow conditions very well.
- The calculated unsteady pressure distribution during controlled vibration matches the associated measurements satisfactorily. On the suction side, the pressure amplitudes are underpredicted in the region characterized by the large separation region.
- The derived overall aerodynamic damping coefficient compares quite well between experiment and numerical analysis, taking into account the relatively large measurement uncertainties on the experimental side, the extreme flow conditions and the linearized Euler solver on the numerical side. Certainly, the present analytical procedure is at a limit, but the test case will be used for future code development.
- It was shown that the calculated aerodynamic damping may become negative under reversed flow conditions at certain operating points, for some IBPA's

7 ACKNOWLEDGMENTS

The work published in this paper was partly funded by the German government within the frame of Lufo 4. This is gratefully appreciated.

8 REFERENCES

[1] Gamache, R. N.; Greitzer, E. M.: "Reverse Flow in Multistage Axial Compressors", AIAA-paper 86-1747, AIAA/ASME/SAE/ASEE 22nd Joint Propulsion Conference, June 16-18, 1986, Huntsville, Alabama

[2] Schoenenborn, H.; Breuer, T.: "Aeroelasticity at Reversed Flow Conditions – Part 2: Application to Compressor Surge", ASME-paper GT2011-45035, Vancouver, Canada, 2011

[3] Bölcs, A.; Körbächer, H.: "Periodicity and Repetivity of Unsteady Measurements of an Annular Turbine Cascade at Off-Design Flow Conditions", AMSE paper 93-GT-107, Cincinnati, Ohio, 1993

[4] Carstens, V.; Bölcs, A.; Körbächer, H.: "Comparison of Experimental and Theoretical Results for Unsteady Transonic Cascade Flow at Design and Off-Design Conditions", AMSE paper 93-GT-100, Cincinnati, Ohio, 1993

[5] He, L.: "Unsteady Flow in Oscillating Turbine Cascade Part 1: Linear Cascade Experiment", ASME-paper 96-GT-374, Birmingham, UK, 1996

[6] He, L.: "Unsteady Flow in Oscillating Turbine Cascade Part 2: Computational Study", ASME-paper 96-GT-375, Birmingham, UK, 1996

[7] Cinnella, P.; De Palma, P.; Pascazio, G.; Napolitano, M.: "A Numerical Method for Turbomachinery Aeroelasticity", J. Turbomach. Volume 126, Issue 2, 310-316

[8] Vogt, D. M.; Fransson, T. H.: "Experimental Investigation of Mode Shape Sensitivity of an Oscillating LPT Cascade at Design and Off-Design Conditions", GT2006-91196, Proceedings of ASME Turbo Expo, May 2006 Barcelona, Spain

[9] Vahdati, M.; Simpson, G.; Imregun, M.: „Unsteady Flow and Aeroelasticity Behaviour of Aero-Engine Core Compressors During Rotating Stall and Surge", GT2006-90308, Proceedings of ASME Turbo Expo, May 2006, Barcelona, Spain

[10] di Mare, L.; Krishnababu, S. K.; Mueck, B.; Imregun, M.: "Aerodynamics and aeroelasticity of a HP compressor during surge and reversed flow", Proceedings of the 12th ISUAAAT, Sept. 1-4, 2009, London, UK

[11] Bölcs, A.: "A Test Facility for the Investigation of Steady and Unsteady Transonic Flows in Annular Cascades", ASME-paper 83-GT34, 1983

[12] Rottmeier, F.: "Experimental Investigation of a Vibrating Axial Turbine Cascade in Presence of Upstream Generated Aerodynamic Gusts", PhD-Thesis No. 2758, Ecole Polytechnique Fédérale de Lausanne, 2003

[13] Belz, J.; Hennings, H.; Kahl, G.: "Experimental Investigation of the Forcing Function and Blades Forced Pitching Oscillations of an Annular Compressor Cascade in Transonic Flow", ASME paper GT2010-23590, Glasgow, GB, June 14-18, 2010

[14] Chenaux, V.; Schoenenborn, H.; Ott, P.: "Experimental Investigations of the Aerodynamics of an Annular Compressor Cascade at Reversed Flow Conditions" Paper submitted for the European Turbine Conference ETC, Istanbul, 2011

[15] Eulitz, F., Engel, K., Nuernberger, D., Schmitt, S., Yamamoto, K.: "On Recent Advances of a Parallel Time-Accurate Navier-Stokes Solver for Unsteady Turbomachinery Flow", Proceedings of the 4th ECCOMAS, Papailiou et al., eds., John Wiley &Sons, Vol. 1, pp. 252-258, 1998.

[16] Nuernberger, D., Eulitz, F., Schmitt, S., Zachcial, A.: "Recent Progress in the Numerical Simulation of Unsteady Viscous Multistage Turbomachinery Flow", ISABE-2001-1081, 2001.

[17] Engel, K.; Zscherp, C.; Wolfrum, N.; Nuernberger, D.; Kuegeler, E.: "CFD Simulations of the TP400 IPC in Off-Design Operating Conditions", ASME-paper GT2009-60324, Orlando, Fl, USA, 2009

[18] Kahl, G.: "Application of the time linearized euler method to flutter and forced response calculations", ASME-paper 95-GT-123, Houston, Texas, June 5-8, 1995

[19] Kahl, G.; Klose, A.: "Computation of time linearized transonic flow in oscillating cascades", ASME-paper 93-GT-269, Cincinnati, Ohio, May 24-27, 1993

[20] Kahl, G.; Hennings, H.: "Computational Investigation of an Oscillating Compressor Cascade Experiment", 9th Symposium on unsteady aerodynamics, aeroacoustics and aeroelasticity of turbomachines (ISUAAAT), Sept. 4-8, 2000, Lyon, France, pp. 819-829

[21] Beretta, A.: "Influence of Mechanical Mistuning on the Forced Response of a Turbine Cascade" PhD-Thesis No. 3608, Ecole Polytechnique Fédérale de Lausanne, 2006

